Welding in the World
https://doi.org/10.1007/s40194-025-02189-x

RESEARCH PAPER

Fatigue assessment of laser hybrid welded butt joints with severe imperfections using 3D scanning and critical distance theory

Mahamudul Hasan Tanvir[1] · **Sulaiman Shojai**[1] · **Richard Banaschik**[2] · **Moritz Braun**[1]

Received: 10 September 2024 / Accepted: 25 September 2025

Abstract

Laser-hybrid welded butt joints are increasingly used in structural applications due to their high productivity. However, the complex interaction between the laser beam and arc process often leads to weld imperfections. These weld imperfections can significantly influence the development of stress concentrations on the weld surface, which can affect the mechanical properties and fatigue performance of the joints. Therefore, accurately identifying and assessing these imperfections is crucial for ensuring weld quality and structural safety. In this study, a method is proposed to assess the weld quality and numerically determine stress concentrations in laser-hybrid welded butt joints with severe imperfections using 3D scans. For this purpose, a total of 76 specimens were scanned using a high-resolution 3D laser scanner to capture the weld geometry. The scan results were then used to assess the weld quality according to the ISO 12932 standard and to generate numerical models by using the reverse engineering method for 3D finite element (FE) analysis. Additionally, fatigue tests were performed to observe the failure location for each specimen and compare it with the predicted failure location from the FE analysis. While the FE predictions could effectively highlight the critical high-stress regions, they did not consistently match the actual crack initiation sites due to the complexity and variability of weld imperfections. However, considering the micro-support effect through the theory of critical distances improved the accuracy of failure location and fatigue life predictions by accounting for the influence of local stress gradients.

Keywords 3D scanning · Laser hybrid welding · Reverse engineering · Weld imperfections · FE analysis · Stress concentration · Butt joints · Fatigue · Micro-support effect

1 Introduction

Laser-hybrid welding is increasingly used to produce high-quality joints in industries such as manufacturing, automotive, shipbuilding, and maritime due to its high productivity and deep penetration capabilities. In structural applications, these welded joints often endure cyclic loading conditions. Therefore, conducting fatigue strength analyses on these joints is crucial to ensure the integrity and safety of welded structures. The fatigue strength of welded joints is frequently evaluated using nominal stress or structural stress approaches. While these methods are well established, they tend to be conservative because they do not adequately account for the actual weld geometry and local imperfections [1]. The presence of various imperfections in the welding zone is a common phenomenon and can significantly impact the fatigue strength of the structures [2–4]. These imperfections tend to amplify local stress concentrations along the weld seam [5, 6]. In laser-hybrid welding, the complex interaction between the laser beam and the arc process often leads to imperfections such as undercuts, worm-holes, and excessive root penetration, each of which can significantly increase local stress concentrations and negatively impact fatigue performance [7, 8].

To improve the fatigue life of welded joints, it is important to identify the critical locations with high local stress concentrations since fatigue failure can initiate from these locations [9–11]. Many promising techniques have been

---

Recommended for publication by Commission XIII - Fatigue of Welded Components and Structures.

✉ Mahamudul Hasan Tanvir
mahamudul.tanvir@dlr.de

[1] German Aerospace Center (DLR), Institute of Maritime Energy Systems, 21502 Geesthacht, Germany

[2] Research & Technology, MEYER WERFT GmbH, Industriegebiet Süd, 26871 Papenburg, Germany

established in recent times for accurately modeling the complex weld geometry in order to perform numerical analysis. One of these approaches involves using 3D scanning to capture detailed information about the weld profile [12, 13]. This technique allows for a more realistic and accurate representation of the weld geometry. The use of 3D weld geometry obtained through various scanning methods can assist in evaluating the fatigue strength of welded joints [14]; however, developing a 3D model for numerical analysis can be difficult due to the complexity of the weld. The use of the reverse engineering method can be useful in transforming the scan results of the complex weld into a solid 3D model for FE analysis. This approach provides the opportunity to develop numerical models with a high degree of accuracy.

Additionally, 3D scanning techniques prove to be useful in gaining a better understanding of the impact of complex three-dimensional weld imperfections on fatigue strength, which cannot be captured by traditional methods [15, 16]. It can also be used to assess the weld quality based on standardized guidelines. ISO 12932:2013 [17] is a commonly used standard for evaluating the weld quality of laser hybrid welded joints, offering guidelines for the permissible limits of different types of weld imperfections based on the geometric characteristics of welds. Although in shipbuilding, the rules of the classification societies are decisive, regarding welding imperfections, these are mainly based on ISO 5817:2023 [18]. However, not all quality assessment criteria and groups have a similar impact on the fatigue properties of the welds, as highlighted by Hobbacher et al. [19]. This is also addressed in Appendix B of ISO 5817:2023 [18].

Previous research has established frameworks for both scanning and simulating weld geometry [13, 20]. Niederwanger et al. [21] conducted a study on various modeling concepts to assess the fatigue strength of welds. Their research utilized a laser scanning process to create 2D models of the weld geometry. Hou [22, 23] found that 3D scanning techniques are a useful tool for analyzing the complex geometry near welded joints. Liinalampi et al. [24] used 3D laser microscopy technology to create a precise representation of the welds and then investigated the fatigue strength of thin plates based on 2D finite element simulation. Chaudhuri et al. [25] applied X-ray micro-computed tomography to capture weld profiles and, combined with ACPD measurements, investigated the fatigue crack initiation (FCI) life of arc-welded joints. Stasiuk et al. [14, 26] conducted research on butt joints and cruciform joints to determine stress concentrations at various areas of the weld toe. They used a scanning process to capture the actual geometry of the joints with higher accuracy. Kolios et al. [27] calculated the stress concentration factor in offshore welded structures based on 3D scan data. The results of their research indicate that this approach can be useful to identify critical areas where fatigue cracks are most likely to initiate. Späth et al. [28] used a 3D FE method to conduct fatigue assessment of welded joints based on the real geometry and proposed a local stress limit of 300 MPa for cruciform joints.

The use of scanning methods is gaining popularity for analyzing welded joints. This technique has been successfully applied previously for surface characterization of additively manufactured components [29, 30] and complex corroded surfaces [31, 32]. However, despite these advancements, the use of 3D scans for fatigue assessment of laser-hybrid welded joints with imperfections has not been thoroughly investigated. This is a notable research gap because laser-hybrid welded joints with several imperfections can be difficult to assess using traditional fatigue assessment methods. Using 3D scans on these joints can help numerically determine local stress concentrations directly and could lead to better fatigue life predictions.

In this study, a methodology is presented that combines 3D scan-based numerical analysis and fatigue assessment to evaluate stress concentrations in laser-hybrid welded butt joints with severe imperfections and to examine their influence on fatigue failure locations. The fatigue assessment incorporates the micro-support effect through the theory of critical distances (TCD) to improve the accuracy of both fatigue life estimation and failure location predictions based on the FE analysis.

This study is structured as follows: Sect. 2 presents the methodology and experimental setup. The numerical modeling process is provided in Sect. 3. Section 4 presents the results and discussion, followed by conclusions in Sect. 6.

2 Methods and experimental setup

2.1 Specimens and fatigue test setup

The specimens were butt welded and made of A36 steel with dimensions of 40 mm in width and 500 mm in length. The welding was carried out by the MEYER WERFT research and development laboratory. A 16-kW disk laser and a metal arc welding process were used. To improve the welding process, these specimens were welded with varying parameters, resulting in the inclusion of severe weld imperfections. A total of 76 specimens were prepared and tested in three test series, with plate thicknesses of 7 mm (Sp. No. 1–31), 10 mm (Sp. No. 32–53), and 15 mm (Sp. No. 54–76). Fatigue tests were performed to identify the failure locations for each of the specimens to compare them with the predicted failure locations from the FE analysis. A Schenck horizontal resonance testing machine with a load capacity of up to 200 kN and a load frequency range of

30–33 Hz was employed for this purpose. Following the experiments, the crack surfaces were visually examined, and the actual failure locations were documented for each of the specimens. The results of the fatigue tests are discussed in Sect. 4.2.

2.2 3D scanning process

The 3D scanning process was carried out with an ATOS GOM Core 5 M scanner with a resolution of 0.12 mm, where resolution refers to the smallest measurable distance between two distinct points on the laser line. The scanner supports measurement volumes ranging from 40 to 800 mm. GOM Inspect software was used for processing the scan results. The scanner is setup in a way that it can cover the whole welded area of the specimen properly (see Fig. 1a). The 3D scanning process comprises two main steps which are the pre-processing and the post-processing.

The pre-processing starts with preparing the specimen by cleaning the surface and adding reference points to both sides of the specimen for aligning the scans during the post-processing stage. This allows to combine the scan results of both surfaces into a single, cohesive model. No additional powder-based coating was used on the specimens to ensure that even small imperfections remained visible. A rotating platform is used to capture the weld surface from different angles (Fig. 1b and c). A total of six scans are performed for each side of the specimen in order to capture the details of the weld surface.

The post-processing of the scan results is carried out by smoothing the areas where small magnets are placed as reference points and merging surface scans using the best-fit command in the GOM Inspect software. The reference points are used to best fit the transformation between the scans and align them in 3D space. The geometry alignment is performed before the final 3D model is exported as STL files. The purpose of the 3D scanning is twofold in this work: to detect and measure the weld imperfections and to create numerical models of the welds for FE analysis.

2.3 Weld quality assessment from 3D scans

Weld imperfections can significantly compromise the strength and reliability of welded joints. The complexity of weld geometry presents a considerable challenge in achieving quality control during welding processes. Various types of imperfections must be assessed when evaluating the quality of a welded joint. Standards in welding, such as ISO 6520–1:2007 [33], offer detailed descriptions of primary welding imperfections and are commonly utilized for their identification. ISO 12932:2013 [17] establishes acceptance criteria for these imperfections, classifying them into three quality groups (B, C, and D) based on their size and type. In this study, samples were assessed using visual inspection and 3D scan results. Four types of imperfections, as defined by the ISO 6520–1 standard, were identified from this assessment. These imperfections are described in Fig. 2.

The relative acceptance limits for the identified weld imperfections, as specified in ISO 12932, are provided in Table 1. During quality assessment, certain imperfections exceeded the tolerance limits defined for the lowest quality group (D) according to the standards. Consequently, these samples were reclassified into quality group “Lower than D.” The process of sample classification into different quality groups and the identification of imperfections are presented in Sect. 4.1.

3 Numerical modeling

In this section, the overall procedure followed to develop the 3D numerical model and carry out the FE analysis is presented. Figure 3 shows a flowchart outlining the steps for the numerical modeling based on the 3D scan.

3.1 Reverse engineering method

The reverse engineering method is used to transform point cloud data obtained from scan results into a solid model suitable for the FE analysis. The commonly exported STL

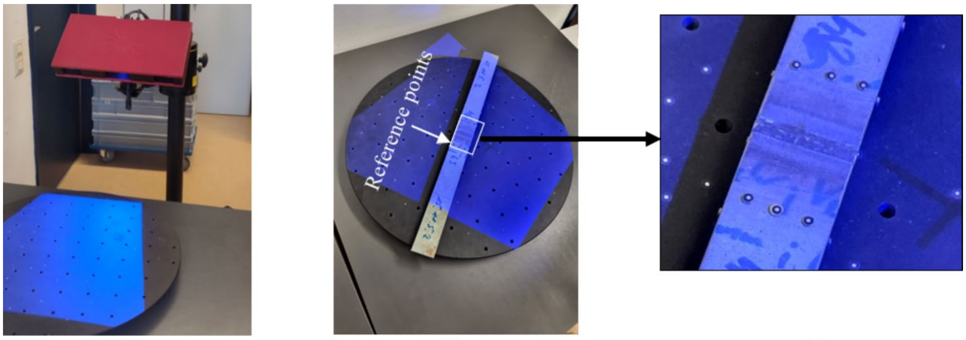

(a) (b) (c)

Fig. 1 3D scanning process: **a** scanner setup, **b** and **c** reference points used in the specimens

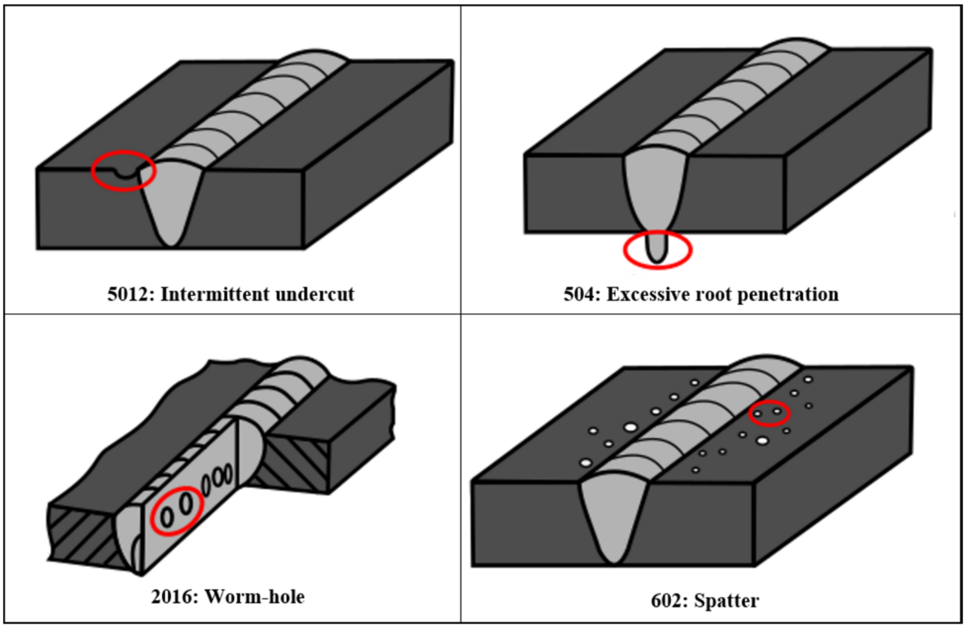

Fig. 2 Weld imperfections identified according to ISO 6520–1 [33] with their corresponding group number

Table 1 Relative limit values of the weld imperfections according to ISO 12932 [17]

Type of imperfection	Quality group		
	B	C	D
Intermittent undercut	0.5 mm (maximum)	0.5 mm (maximum)	1 mm (maximum)
Excessive root penetration	3 mm (maximum)	4 mm (maximum)	5 mm (maximum)
Worm-hole	2 mm (for 10 mm plate thickness)	3 mm (for 10 mm plate thickness)	4 mm (for 10 mm plate thickness)
Spatter	Acceptance depends on application	Acceptance depends on application	Acceptance depends on application

format from scan results lacks surface curvature continuity, potentially leading to singularity issues during FE analysis [31]. To overcome this challenge, the model can be converted into a smoother representation using Non-Uniform Rational B-Spline (NURBS) surfaces. NURBS is a mathematical representation of 2D smooth surfaces widely utilized in 3D modeling, particularly in the reverse engineering process. It offers a precise means of representing and manipulating complex shapes using a relatively small number of control points. Additionally, NURBS surfaces require less data to describe the surface compared to the STL format which makes it efficient for storage and transmission. In this work, the Ansys 2022 R1 software is used for executing the reverse engineering method and conducting FE analysis.

The accuracy of the fit between the scanned data and the modeled surface in the reverse engineering process is determined by the use of the polynomial functions during the modeling process. In Ansys SpaceClaim, polynomial functions are controlled by the sample size. The larger the sample size, the more polynomial functions will be used per area, resulting in a better fit between the scanned data and the modeled surface. However, a larger sample size also increases the computational time and memory requirements. The polynomial fitting is based on cubic B-spline functions with a degree of 3 and an order of 4, consistent with the underlying NURBS representation. Creating a solid model using a single NURBS surface is not possible because of the complexity of the weld surface; as a result, the surface is broken down into smaller portions called NURBS patches. These patches are then joined together to form the solid model. The choice of the sample size is determined by the geometry and quality of the scanned surface. In previous studies, Shojai et al. used a sample size of 120 grids per 15 mm length in [31] and a sample size of 120 grids per 40 mm length in [32]. In this work, a sample size of 105 grids is utilized, and the size of the patch is adjusted based on the complexity of the geometry, in order to capture the welded area with higher accuracy. In Fig. 4, an example of using different sample sizes for the same surface geometry is shown. The surface details are more accurately captured with a larger sample size. In Fig. 5, the original surface of specimen No. 33 is compared with the 3D scanned surface

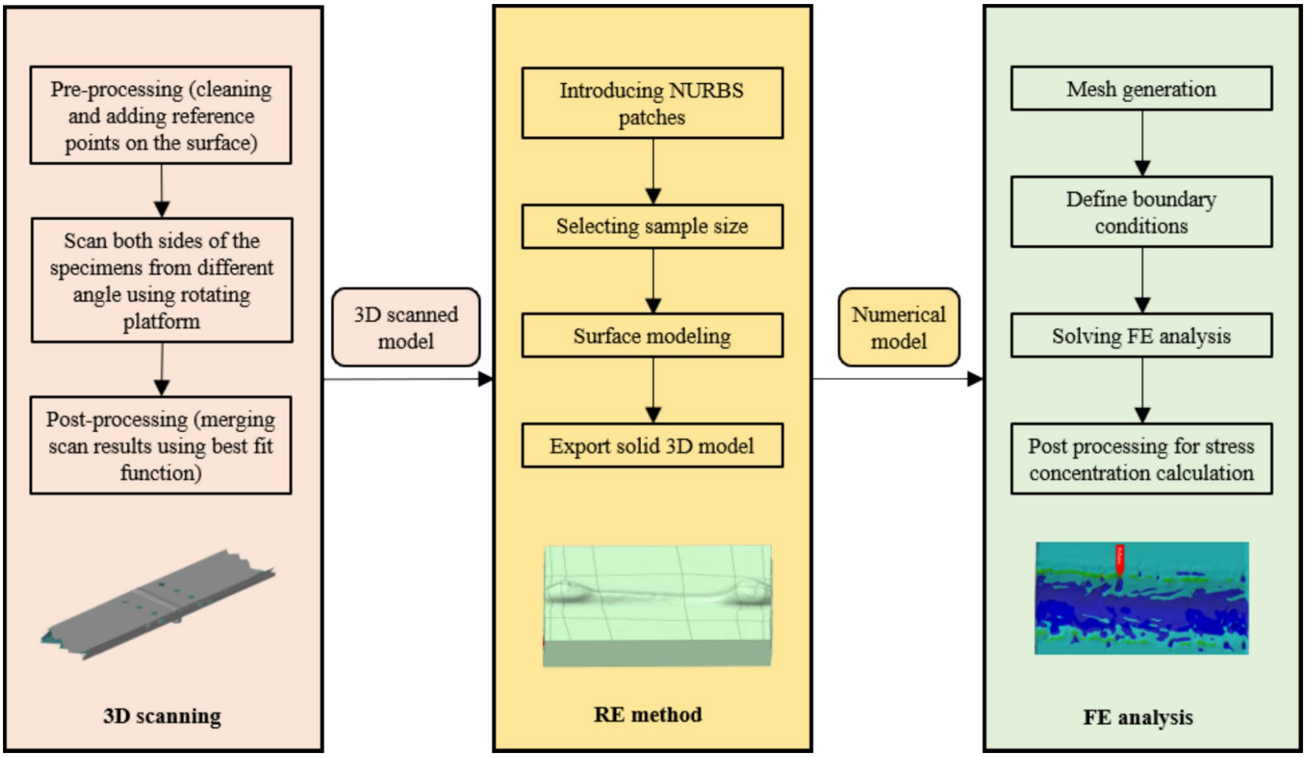

Fig. 3 Flow chart of 3D modeling and FE analysis process

Fig. 4 NURBS patch of a 15 × 15 mm sample with sample sizes 15, 50, and 105 (from left to right)

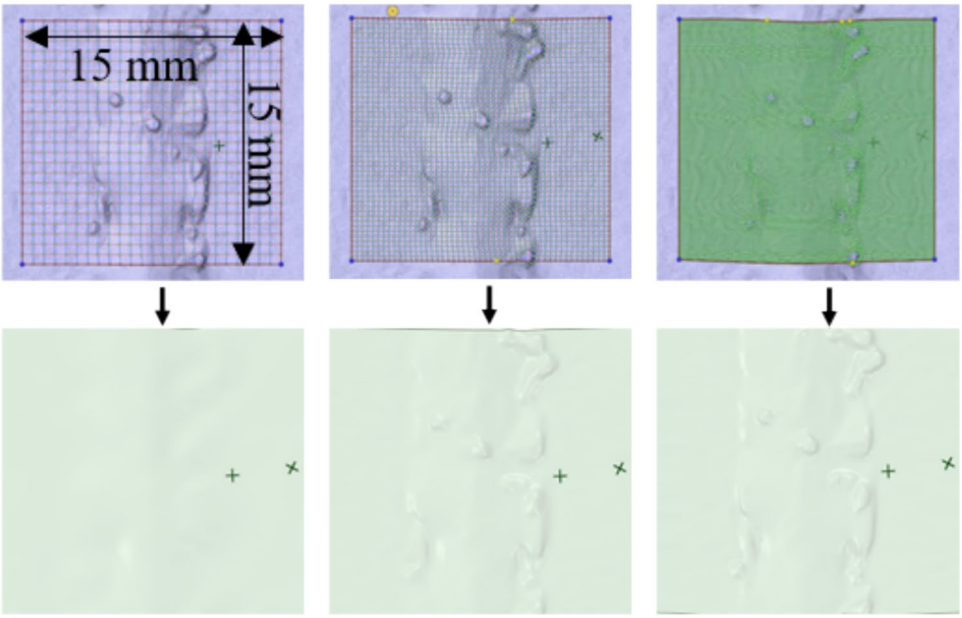

and the output result of the reverse engineering method. Additionally, in Fig. 6, the faceted geometry alongside the final numerical model for specimen No. 09 is provided to compare the deviation of the surface geometry. It is observed that the details of the weld geometry can be captured and transformed accurately into the numerical model by applying the reverse engineering method.

3.2 Numerical model and boundary condition

The 3D models generated by the reverse engineering method are imported into the Ansys Workbench, as shown in Fig. 7. Structural steel with a Young's modulus of 200 GPa, a Poisson's ratio of 0.3, and a linear-elastic material model is used for the analysis. This is possible, since stress concentration

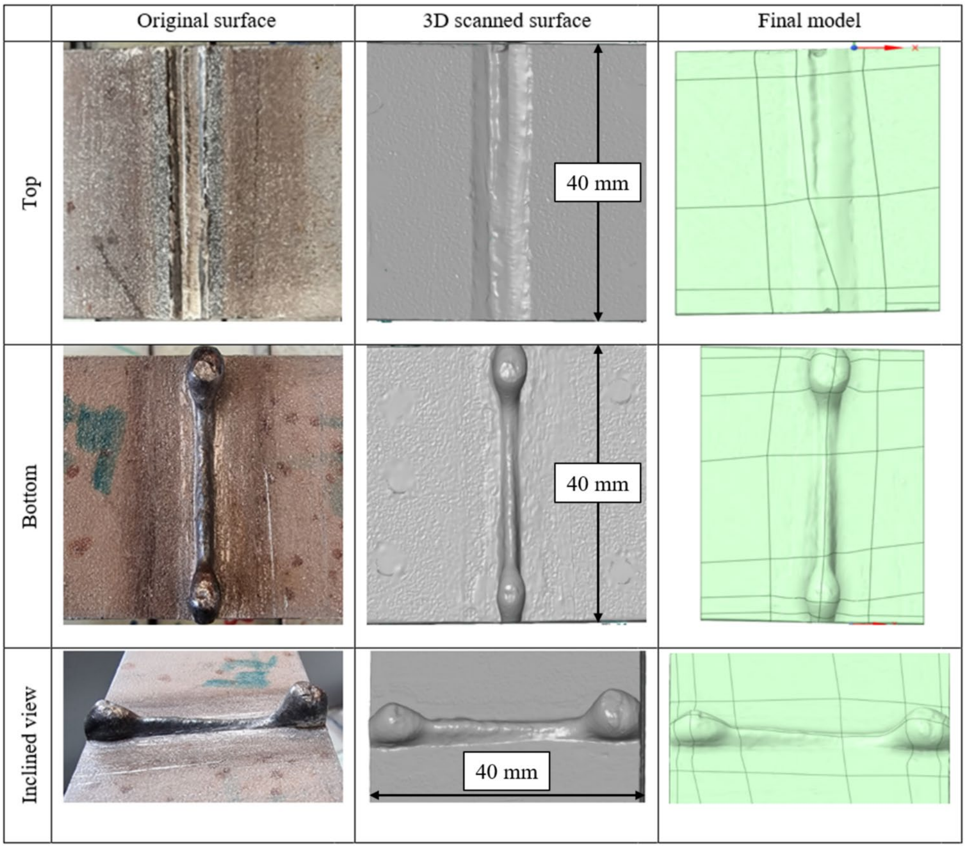

Fig. 5 Comparison of the scanning results and the numerical model with the actual surface of specimen No. 33 (with excessive root penetration defect)

value on the surface does not depend on the material properties, but rather on the geometry of the object and the location and type of the applied loads.

The boundary conditions used for the FE analysis are represented schematically in Fig. 7. To apply the boundary condition, a remote displacement was applied to one side of the specimen, and a load was applied to the opposite side. The displacement in the loading direction was restricted, and one node in the transverse direction was also confined. The load was adjusted based on each specimen's cross-sectional area to achieve a nominal stress (σ_{nom}) of 1 MPa, ensuring that the maximum stress (σ_{max}) results on the surface are equivalent to the stress concentrations (K_t) of that specimen according to Eq. 1.

$$K_t = \frac{\sigma_{max}}{\sigma_{nom}} \tag{1}$$

3.3 Mesh generation and convergence study

The imperfections presented on the weld surface make the mesh generation process quite challenging. The quadratic tetrahedral elements were used for the meshing process. The element size selection during meshing is an important factor in ensuring the accuracy of the FE analysis, and for this, the mesh sensitivity analysis is performed. Figure 8a–c show the effect of varying element size on the ability to accurately capture the geometric details. The results from the sensitivity analysis have shown that a 0.1–0.2 mm element size is sufficient for maintaining consistency in the location of maximum stress concentration on the weld surface. Therefore, an element size of 0.1 mm has been used close to the welded zone for each specimen, and a coarser mesh size of 2.97 mm is used for the remaining surface.

To further improve accuracy and reduce computational cost, convergence analysis was performed only in regions of maximum stress concentration. Additional refinement in these areas was achieved using the adaptive convergence tool in Ansys Workbench. For example, in specimen No. 03, a minimum element size of 0.026 mm was reached at the peak stress location, with surrounding elements ranging from 0.03 to 0.1 mm. As shown in Fig. 8d, the maximum stress value remained constant with this level of refinement.

4 Result and discussion

4.1 Weld quality assessment results

The weld quality assessment results, along with corresponding measurements of weld imperfections and the determined

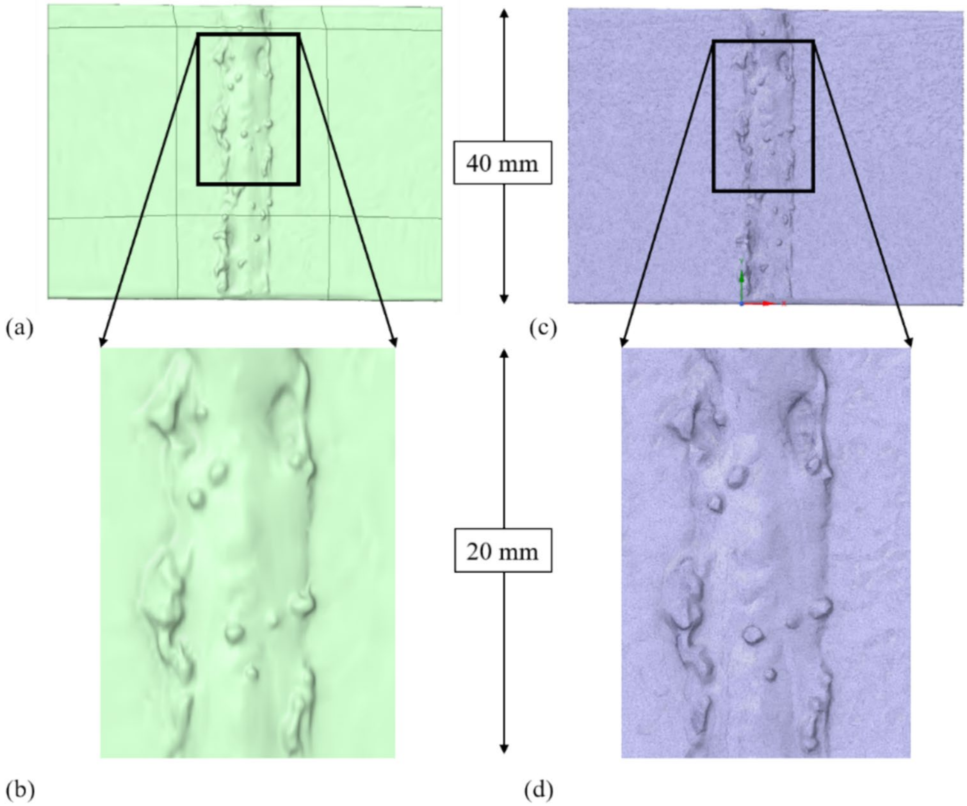

Fig. 6 Specimen No.09: **a** and **b** numerical model, **c** and **d** faceted geometry from 3D scan

quality groups, are summarized in Appendix B, Table 6. The quality group of each specimen is determined based on the relative limit values of each weld imperfection presented in Sect. 2.3. The 3D scan results of each specimen were used to detect and measure imperfections such as intermittent undercut (Fig. 9b) and excessive root penetration (Fig. 9d). GOM Inspect software was used to measure the dimensions of these imperfections from the scan results. The worm-hole imperfection was identified from the cracked surface images taken post-fatigue testing of each specimen, and the dimension of the largest worm-hole was measured from these images. It is important to note that the worm-hole imperfection was not included in the FE modeling. The measurement process for the worm-hole imperfection is presented in Fig. 9a. Additionally, visual inspections of the welds were performed to identify spatter on the weld surfaces (Fig. 9c). Out of the 76 specimens studied, 45 were classified in weld quality group B, 4 in group C, 9 in group D, and 18 in group "Lower than D."

4.2 Fatigue test results for different quality groups

The fatigue test results for each of the specimens are presented in Appendix A, Table 5. The results are analyzed statistically to generate S–N curves for different weld quality groups with:

$$N_f = 2 \times 10^6 \left(\frac{\Delta\sigma_{nom}}{\Delta\sigma_R}\right)^{-m} \tag{2}$$

where N_f represents the number of cycles to failure, $\Delta\sigma_{nom}$ is the nominal stress range used during the experimentation, $\Delta\sigma_R$ states as the characteristic reference fatigue strength at $N_f = 2 \times 10^6$ cycle, and m is the slope of the S–N curve.

The mean curve for the S–N diagram is determined by following the guidelines of the German Welding Society (DVS) [34], which state that a least-square algorithm should be used for the curve fitting. The mean curve represents a survival probability of $P_S = 50\%$. In accordance with international guidelines, a consistent slope of $m = 3$ is utilized for all standard design curves [35]. In order to maintain consistency and comparability of the S–N curves across the different weld quality groups in this study, a fixed slope of $m = 3$ was utilized when comparing the results with the standard design curves. Additionally, only specimens that failed before reaching 2 million cycles were considered, as this cycle count represents the approximate knee point of S–N curves of welded joints [35].

The fatigue test results for different weld quality groups are plotted in a S–N diagram shown in Fig. 10. The results indicated that the average fatigue strength for quality group "Lower than D" is significantly lower than other quality groups. The mean fatigue strength values for groups B and D are similar, but there are fewer specimens in group D ($n = 9$)

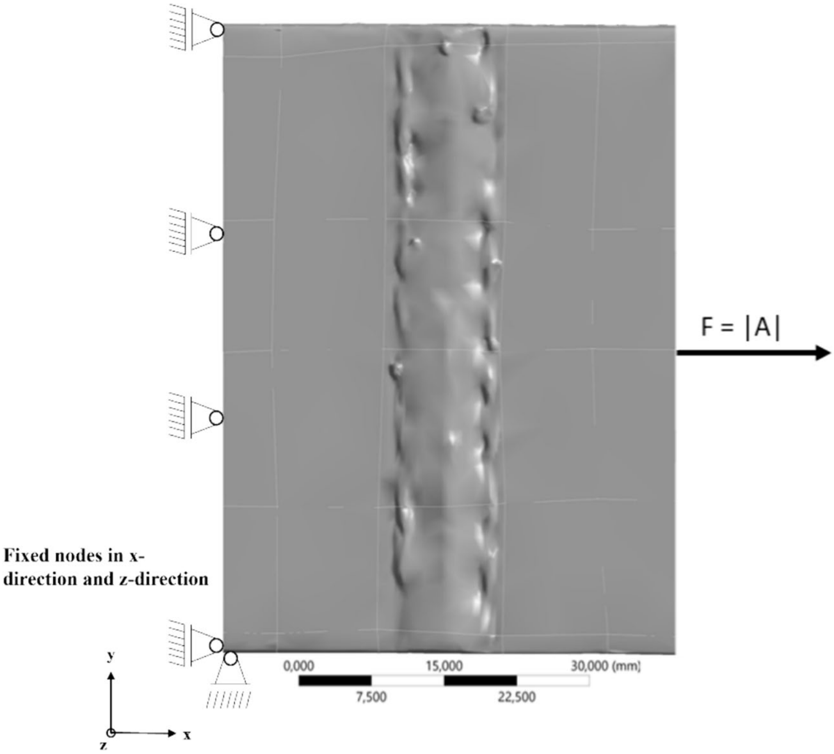

Fig. 7 Boundary conditions of the numerical analysis

which might cause uncertainty in the result. In contrast, the specimens belonging to quality group C have a higher mean fatigue strength value than groups B and D. However, only 4 specimens are categorized in quality group C which might not be sufficient to determine the mean fatigue strength value reliably. In the quality group "Lower than D," worm-hole, undercuts, and excessive root penetration imperfections were found. It is assumed that these imperfections are causing the significantly low fatigue strength of this group.

The S–N plot results further show that the mean fatigue strength for all quality groups exceeds FAT 90. Appendix B of ISO 5817:2023 provides limit values for weld imperfections that correlate quality group B with at least FAT 90 and group C with at least FAT 63, but lacks guidance for groups D and "Lower than D." This study's results validate the relationship between quality groups B and C and their corresponding FAT classes per ISO 5817:2023. However, it also highlights that fatigue strength does not decrease significantly for lower quality groups such as D and "Lower than D." The S–N curve parameters for different weld quality groups are provided in Table 2.

4.3 FE analysis results

The FE analysis is carried out for all the specimens to identify critical areas with high stress concentrations where fatigue failure is likely to initiate. The maximum local stress concentration on the weld surface is determined from the simulation results. Additionally, the stress concentration value at the actual failure location is determined for each specimen. The coincidence level of the predicted failure location from the FE analysis with the actual failure location is categorized into the following four comparison groups.

- Group 1: In this group, the ratio between the stress concentration value at the actual failure location ($K_{t,crack}$) and the maximum stress ($K_{t,max}$) value from the FE analysis is 1. That means the location of the maximum stress concentration in the model coincides with the actual failure location.
- Group 2: In this group, the ratio between the $K_{t,crack}$ and $K_{t,max}$ is higher than 0.75. That means the crack location coincides with the second highest stress concentration value from the numerical model.
- Group 3: In this group, the ratio between the $K_{t,crack}$ and $K_{t,max}$ is higher than 0.5. That means the crack location coincides with the third and the fourth highest stress concentration values from the numerical model.
- Group 4: In this group, the ratio between the $K_{t,crack}$ and $K_{t,max}$ is lower than 0.5. This group indicates a significantly lower correlation between the actual and predicted failure locations.

An illustration of the results from each of the comparison groups is provided in Fig. 11a–d. Moreover, all the comparisons of failure locations with the predicted results from

Fig. 8 Meshing at different element sizes: **a** 0.1 mm, **b** 1 mm, **c** 1.5 mm. **d** Convergence plot for specimen No. 03

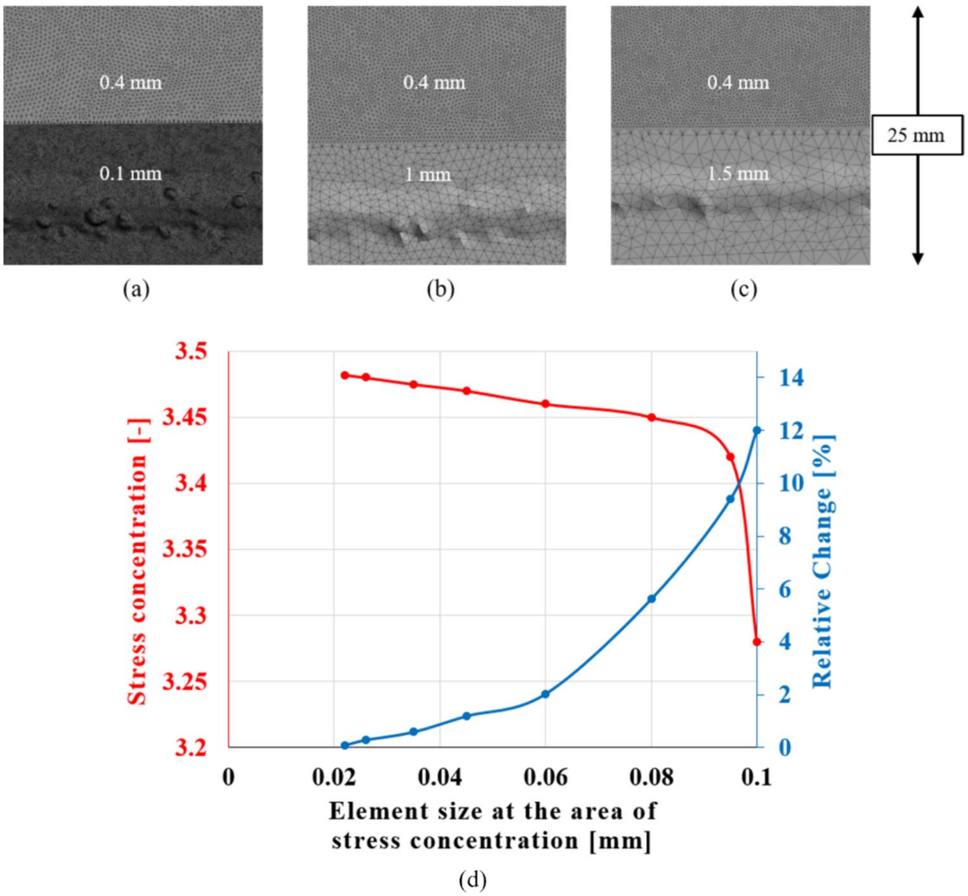

Fig. 9 Weld quality assessment: **a** worm-hole measurement for Sp. No. 41, **b** intermittent undercut measurement for Sp. No. 63, **c** spatter identification for Sp. No. 09, **d** excessive root penetration measurement for Sp. No. 54

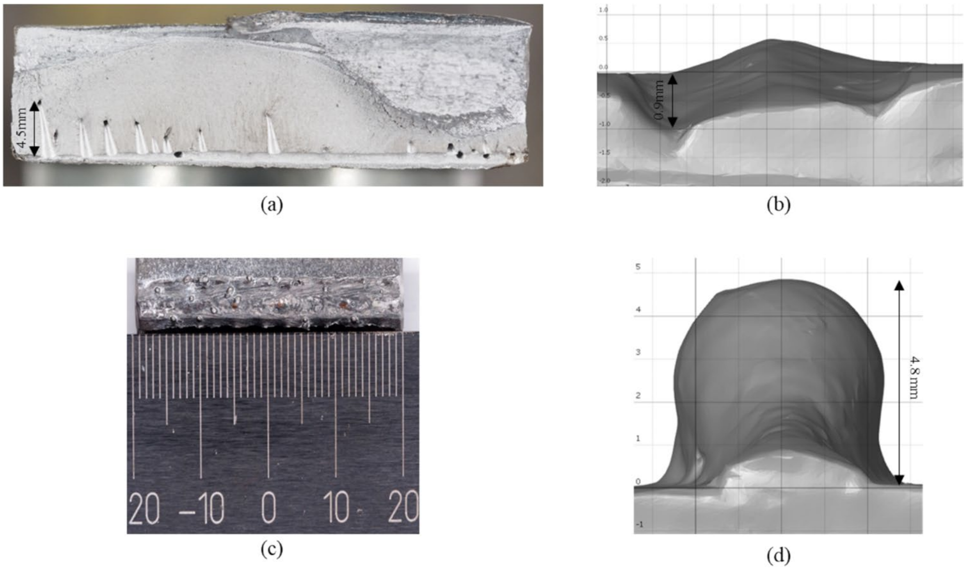

the FE analysis are provided in Appendix C (Figs. 16–19). The blue markings on the figures indicate the actual fatigue failure location, while the red markings show the location of the maximum stress concentrations on the surface, which is the predicted failure location according to the FE analysis.

For specimen No. 50 in Fig. 11a, the predicted failure location from the FE analysis coincides with the actual failure location. The crack surface indicated that the failure was initiated in the weld toe region, where the maximum stress value is observed from the FE analysis. Out of the

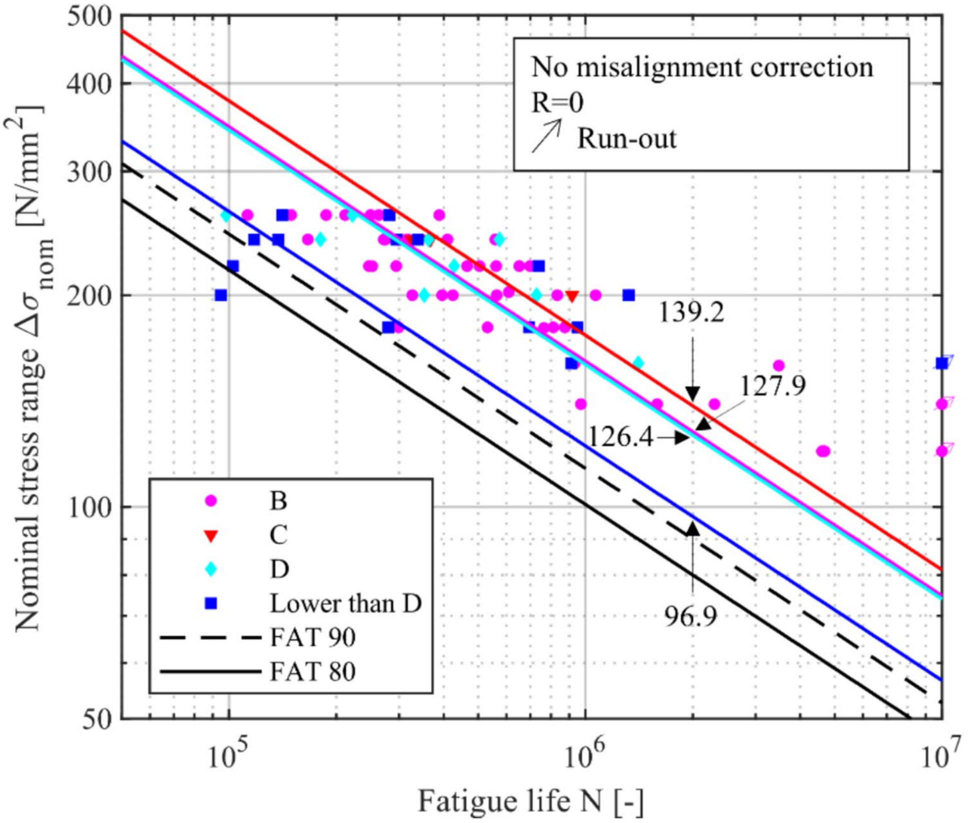

Fig. 10 Fatigue test results for different weld quality groups

Table 2 S–N curve parameters

Group	Slope	Standard deviation	$\Delta\sigma_{R,50\%}$ (MPa)
B	3	0.41	127.9
C		1.65	139.2
D		1.16	126.4
Lower than D		1.71	96.9

76 specimens used for the FE analysis, only 9 specimens fell into this group, with 6 of them belonging to the weld quality group B.

In Fig. 11b, the result for specimen No.02 is shown, which is categorized as group 2. The numerical model determines the maximum stress concentration value of 2.66 at the weld toe region of this specimen. However, it does not match with the actual failure location as the visual inspection of the crack surface indicated that the failure was initiated at the weld root region. The stress concentration value at the actual failure location from the model was found to be 2.44, which gives the stress ratio of 0.92, and hence, it is in group 2. A total of 22 specimens out of 76 belong to this group, including 15 from the weld quality group B. Groups 3 and 4 follow similar patterns. In Fig. 11c and d, the stress ratios for the actual and predicted failure locations are 0.6 and 0.25, respectively. This means that specimen No. 54 is in group 3, and specimen No.47 is in group 4. After analyzing the results, it was found that 29 specimens belong to group 3, and 16 belong to group 4.

Among the 76 specimens analyzed in this study, 60 belong to groups 1–3, where the crack locations align with regions of relatively high stress concentration. The difference between the predicted and actual crack locations for specimens other than those in group 1 is assumed to be due to local structural support mechanisms, such as micro-structural effects. This can be considered with the TCD method summarized by Taylor [36, 37]. According to Taylor, the fatigue-driving stress is not the peak stress on the surface, but rather the stress in a certain distance from the peak. In Fig. 12a, the stress concentration for a representative specimen of group 2 is plotted for both the crack location as well as the maximum stress location in the thickness direction. The results indicate that the stresses at the crack location exceed those at the maximum stress location at a distance of 0.008 mm from the surface. This so-called “shifting point” can also be observed for a representative specimen of group 3 at a distance of 0.018 mm from the surface (see Fig. 12b). The observed shifting point is crucial, as it represents a transition from the initial maximum stress concentration to a region where stress accumulation at the crack site becomes more significant.

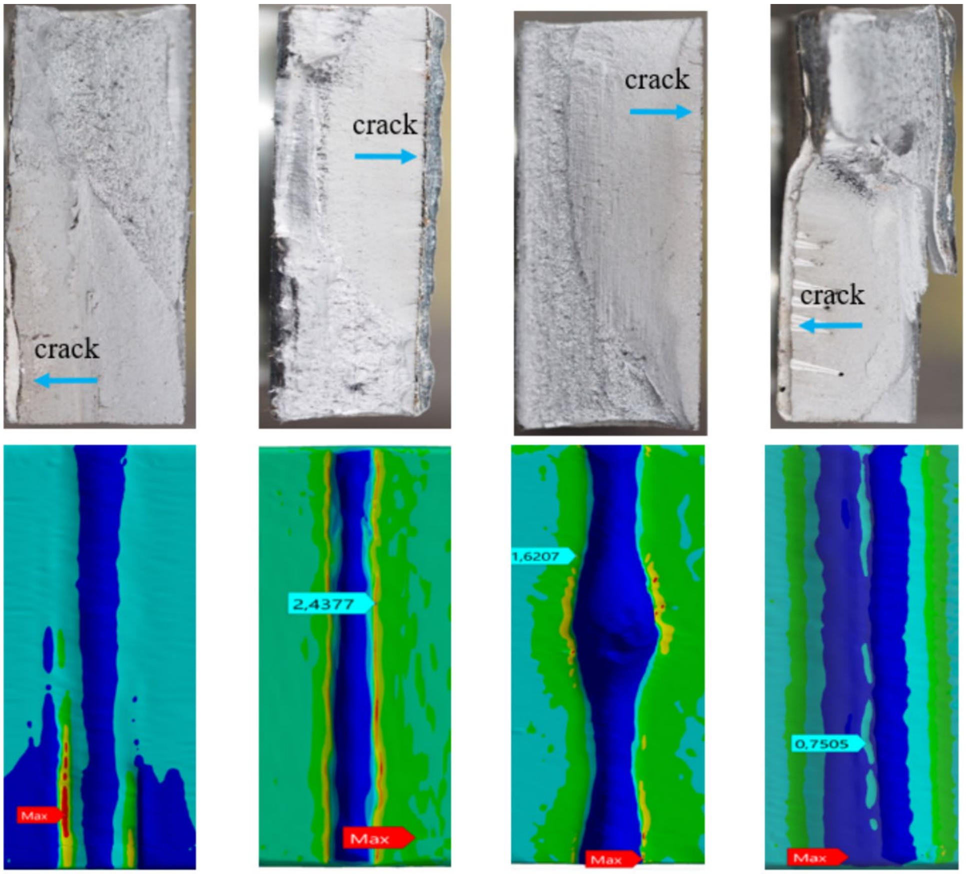

(a) Sp.No. 50 (b) Sp.No. 02 (c) Sp.No. 54 (d) Sp.No. 47

Fig. 11 Comparison of FE analysis results with actual failure location. **a** group 1, **b** group 2, **c** group 3, **d** group 4

These findings align with previous research on predicting fatigue failure locations based on stress distribution on the surface. Taylor et al. [38] studied components with multiple stress-concentrating features and found that failure can occur at a location other than the one experiencing the highest stress on the surface. Similarly, Shojai et al. [39] also observed that differences between predicted and actual crack locations may result from stress gradients along the thickness, indicating the influence of micro-support effects.

Furthermore, the deviation in the predicted failure location from FE analysis could also be influenced by the presence of multiple weld imperfections. From the 3D scans, weld imperfections such as undercuts, surface spatter, and excessive root penetration are found in some specimens. Additionally, worm-holes are observed by inspecting the crack surfaces of the welds after fatigue testing, see Fig. 11d. The numerical models in this study only evaluated the maximum stress concentration based on the specimen's external geometry and did not account for internal defects like worm-holes. Other imperfections, such as undercuts, excessive root penetration, and spatter on the weld surface, may also contribute to the crack formation process, potentially causing unexpected fatigue failure in the specimens. The frequency plot of these various weld imperfections and the coincidence group is presented in Fig. 13a and b. These imperfections can greatly influence the fatigue strength of the welded joints and initiate the fatigue failure due to the high local stress concentrations. The results of the FE analysis, along with the identified imperfection on the weld surface for each specimen, are provided in Appendix A, Table 5.

From the results of the FE analysis, a S–N curve is generated for the specimens without internal imperfection (worm-hole). The S–N curve for different coincidence groups with a fixed slope ($m = 3$) is presented in Fig. 14. The results demonstrate a substantial scatter ratio, with multiple crack initiation sites observed in many specimens during the examination of the crack surfaces. It is assumed that this may contribute to the higher scatter ratio. The S–N curve parameters for different coincidence groups are provided in Table 3.

4.4 Fatigue assessment with the theory of critical distance

As shown in Fig. 12, the location of maximum stress in a specimen can shift when the micro-support effect is taken into account. This happens because the stress gradient is

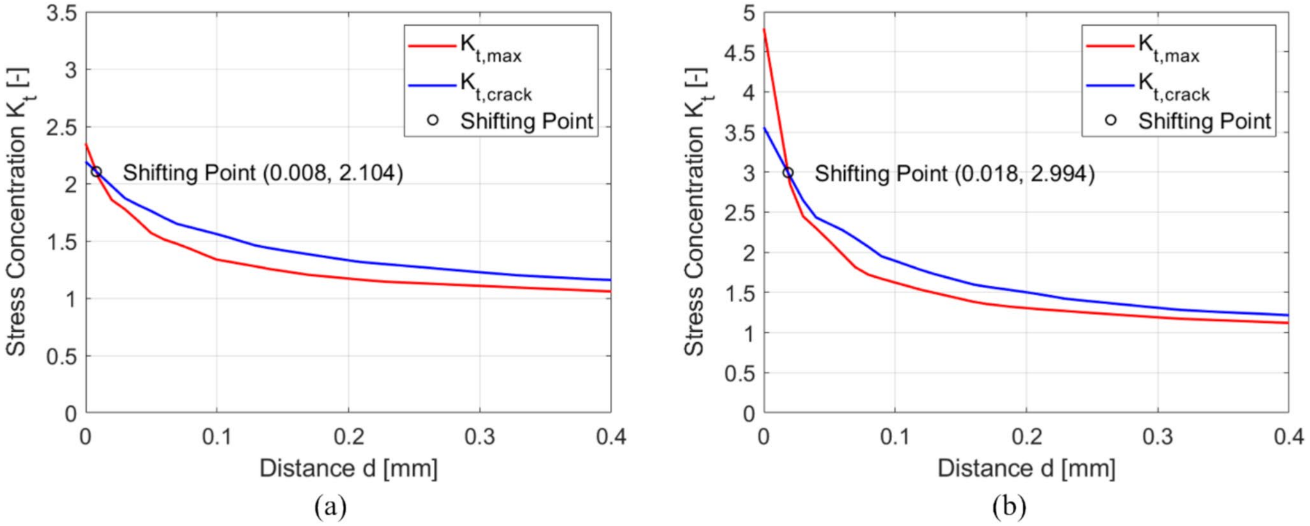

Fig. 12 Stress concentration in the thickness direction for maximum stress concentration and crack initiation location. **a** Sp. No 67 (group 2), **b** Sp. No 01 (group 3)

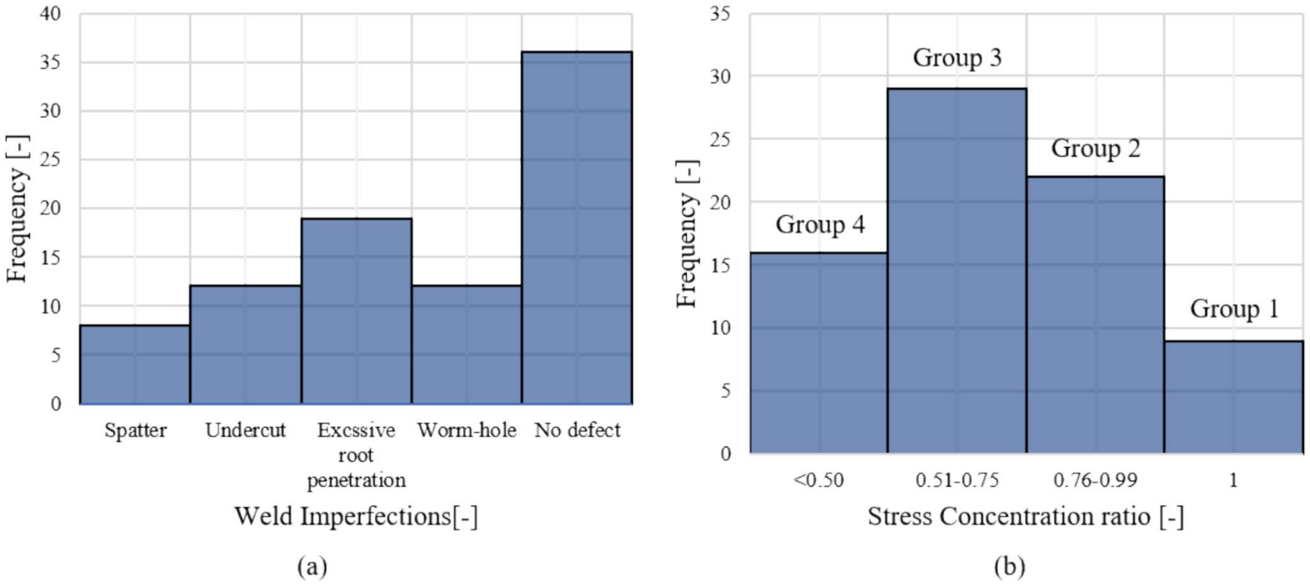

Fig. 13 Frequency plot: **a** weld imperfections identified from 3D scans, **b** coincidence group

not uniform and varies depending on the position within the specimen. To further evaluate the influence of the micro-support effect, TCD was applied at both the crack location and the location of maximum notch stress for all 60 specimens in groups 1 to 3. Taylor [36] introduced TCD by combining the critical distance method (point method, PM) by Peterson [40] and the stress averaging approach (line method, LM) by Neuber [41]. Both methods use a characteristic material length to describe how stress is distributed near notches.

The PM evaluates the stress at a specific distance *d* from the surface according to the following equation:

$$\sigma_e = \sigma_k(x = d) \quad (3)$$

Where σ_e is the effective notch stress and σ_k is the local notch stress.

The stress averaging approach from Neuber [41] determines the effective stress by averaging the notch stress over a microstructural length $\rho*$ along the direction of the stress gradient. The effective notch stress is calculated as follows:

$$\sigma_e = \frac{1}{\rho^*}\int_0^{\rho^*} \sigma_k(x)dx \quad (4)$$

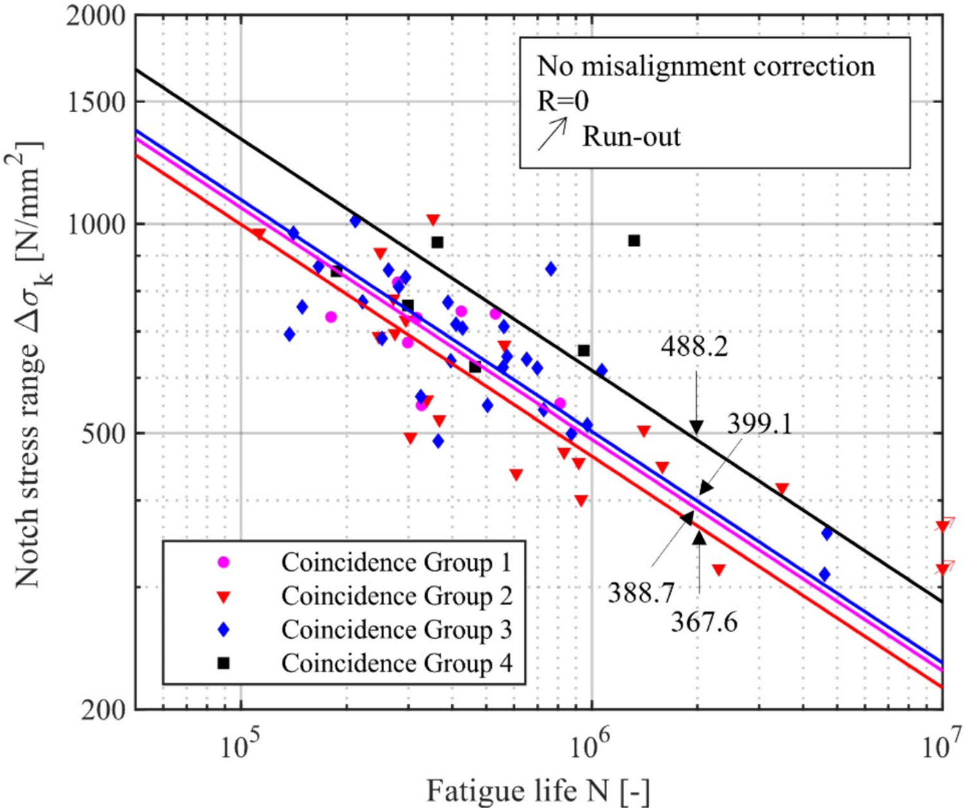

Fig. 14 S–N curve based on the effective notch stress method for different coincidence groups

The characteristic lengths for the point method d and the line method ρ^* were identified using a scatter minimization technique, as applied in previous studies [39, 42]. Each parameter was iteratively varied within a range of 0 to 1 mm to determine the values that resulted in the lowest scatter in the S–N curves, based on the maximum principal stresses. Additionally, a conformity analysis was carried out to assess how often the stress at the crack location exceeded the stress at the maximum stress location. This was evaluated using the ratio of the notch stresses, defined as $r_{conf} = K_{t,crack}/K_{t,max}$.

Figure 15a and d show the relationship between the scatter T_σ and the parameters d and ρ^*, as derived from the scatter minimization process. For the point method, although the minimum scatter is observed at $d=0.10$ mm, a second decrease in scatter is also observed at a higher range of d (≥ 0.5 mm). In the case of the line method, the scatter remains relatively stable in the range 0.25 mm $\leq \rho^* \leq$ 1 mm, suggesting that values within this interval would provide similar assessment results. To remain consistent with previous studies and recommendations for steel components and the maximum principal stress criterion, a critical distance of $d=0.1$ mm and a microstructural length of $\rho^*=0.4$ mm [42] were chosen. This resulted in a scatter of $T_\sigma=1.66$ for PM and $T_\sigma=1.64$ for LM, respectively.

The corresponding S–N curves based on the notch stresses for the selected characteristic lengths for the point method and the line method are shown in Fig. 15b and e. The statistical evaluation was carried out using Deming regression, which accounts for uncertainties in both the stress range and the number of cycles to failure. Based on the analysis, the resulting fatigue resistance at two million load cycles with a 97.7% survival probability is $\Delta\sigma_c=167$ N/mm^2 with a slope of $m=5.1$ for the point method, and $\Delta\sigma_c=154$ N/mm^2 with a slope of $m=5.28$ for the line method. At the selected characteristic lengths, the conformity rate was approximately 65%. Although a higher conformity rate was observed at larger values of these parameters, those values lie outside the range where the scatter is minimized. Using such values could compromise the reliability of S–N curve fitting and fatigue life assessment. Based on these findings, a design FAT class of 160 could be recommended to use for the fatigue assessment with a slope of $m=5$, as this value provides the best fit to the experimental data and aligns with

Table 3 S–N curve parameter based on the effective notch stress method

Coincidence group	Slope	Standard deviation	Scatter, T_σ	$\Delta\sigma_{R,50\%}$ (MPa)
1	3	1.30	1.54	388.7
2		0.51	1.67	367.6
3		0.53	1.58	399.1
4		2.45	2.32	488.2

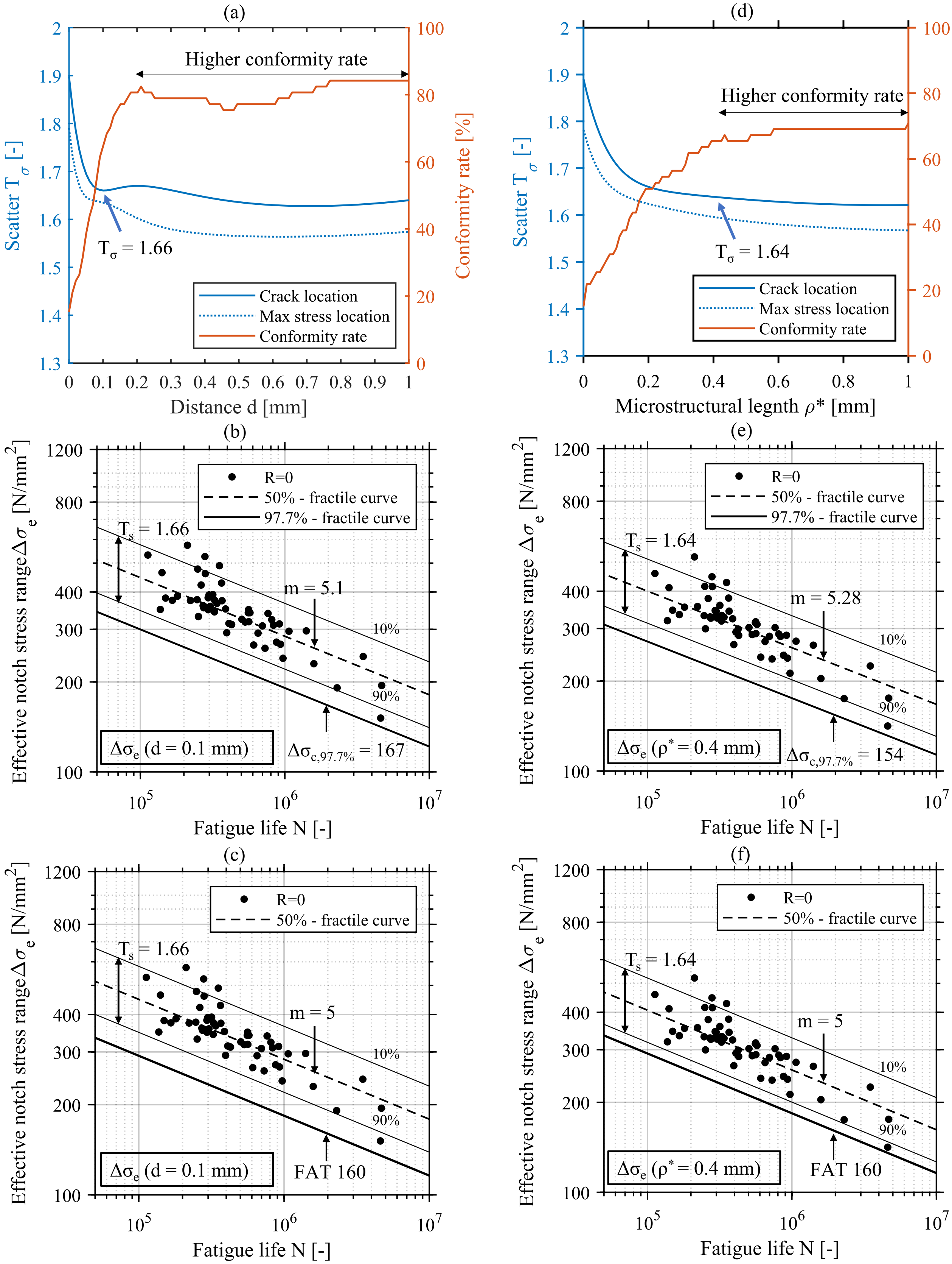

Fig. 15 Results from the TCD methods: **a–c** point method, **d–f** line method. **a**, **d** Scatter plots; **b**, **e** S–N curves with free slope; **c**, **f** S–N curves with fixed slope ($m = 5$)

Table 4 S–N curve parameters with micro-support consideration

Methods	Free slope	$\Delta\sigma_{c,97.7\%}$ (N/mm^2)	Scatter, T_σ	Fixed slope	$\Delta\sigma_{c,97.7\%}$ (N/mm^2)	Scatter, T_σ
Critical distance	5.1	167	1.66	5	166	1.66
Stress averaging	5.28	154	1.64	5	152	1.64

the observed scatter range. The resulting S–N curves based on a slope of 5 are shown in Fig. 15c and f. A summary of the resulting S–N characteristics is provided in Table 4.

A similar evaluation was performed using the stress gradients from the maximum stress location, without considering the actual crack initiation sites, as these are usually not known without experimental investigations. The resulting scatter (see Fig. 15a and d) followed a comparable trend, with slightly improved values: $T_\sigma = 1.63$ for the point method and $T_\sigma = 1.6$, both at $d = 0.1$ mm and $\rho^* = 0.4$ mm. These results are close to those obtained using the stress gradients from the crack location and would lead to comparable fatigue life predictions.

5 Discussion

In this study, 3D scanning and reverse engineering methods were applied to assess weld quality and fatigue assessment of laser hybrid welded butt joints with severe imperfections. The 3D scan results were used to identify and measure weld imperfections, enabling the classification of weld quality groups according to the ISO 12932 standard. The fatigue strength of these groups was then compared to standard FAT classes. The numerical model developed through this approach effectively captures weld details. This method has the potential to eliminate the need for idealized weld geometry in numerical analysis. However, the results of the FE analysis indicated that the crack locations of the majority of the specimens (groups 1–3) coincided with areas of relatively high stress, but did not always match with the absolute maximum stress location. Further investigations of the stress gradient along the thickness of these specimens were carried out using the TCD method to assess whether considering the micro-support effect could improve the prediction of crack location and enhance fatigue assessment. Based on a scatter minimization approach, a critical distance of $d = 0.1$ mm and a microstructural length of $\rho^* = 0.4$ mm were selected. For welded joints, these values are consistent with previous recommendations [42]. The conformity rate at these parameters was about 65%, indicating that 39 out of 60 specimens showed agreement between the predicted and actual crack locations at the selected characteristic lengths ($\rho^* = 0.4$ mm and $d = 0.1$ mm). This suggests that considering the micro-support effect can improve the prediction of crack initiation sites. It is important to note that the TCD method evaluated the effective stresses at only two locations: the actual crack location and the location of maximum stress. If the TCD method were applied across all surface points, the maximum effective stress could shift to a location different from the two points evaluated here.

The implicit gradient method [39] offers a potential solution to this limitation, as it considers the micro-support effect directly in the numerical analysis for all surface points simultaneously. This enables a more comprehensive assessment of the effective stresses. As shown in [39], such approaches could further enhance the conformity rate and improve fatigue assessment. However, it is also important to consider that S–N curves based only on the stress gradient at the location of maximum stress showed minimal variation in fatigue life prediction and associated scatter, even without knowing the exact crack initiation site. This suggests that, for fatigue life prediction purposes, using the stress gradient at the maximum stress location may be sufficient, even if the actual crack location is unknown.

For a reliable fatigue assessment, a design S–N curve is essential. Based on the findings of this study, a FAT class of 160 is recommended when applying the TCD method, which aligns with the design FAT class proposed by Baumgartner [42]. Regarding the slope of the S–N curve, the analysis indicates that a slope of $m = 5$ provides the best fit to the experimental data. Although a slope of $m = 3$ [43] is commonly recommended for thick specimens ($t \geq 4$ mm), previous studies have also supported the use of $m = 4$ [42]. However, in this study, a slope of $m = 5$ is found to be more appropriate for capturing the fatigue behavior. It should be noted that the statistical evaluation was performed using Deming regression, which offered a better fit and more reliable coverage of the experimental data of this study compared to other regression methods.

6 Conclusion

The aim of this study was to assess the fatigue performance of laser hybrid welded butt joints with severe weld imperfections using 3D scanning and the critical distance approaches. The key findings of this study are summarized as follows:

- 3D scanning process can be useful to analyze the weld quality by identifying the weld imperfections and develop numerical models based on real weld geometry using the reverse engineering method.
- The fatigue test results validate the correlation between quality groups B and C and their corresponding FAT classes according to ISO 5817:2023 (Appendix B), while also demonstrating that fatigue strength does not significantly decrease for lower-quality groups such as D and "Lower than D."
- FE analysis results indicate that it can be useful for effectively locating critical high-stress areas that are susceptible to fatigue failure. The crack location of the majority (60 out of 76 specimens) of the specimens coincides with relatively high-stressed areas (groups 1 to 3). For 9 specimens (group 1), the crack location even coincided with the absolutely highest stressed area.
- To consider the micro-support effect, the TCD method was applied to 60 specimens from groups 1 to 3. A critical distance of $d = 0.1$ mm and a microstructural length of $\rho^* = 0.4$ mm were determined based on the maximum principal stresses. At these parameters, the conformity rate increased from an initial 15% to about 65%, suggesting that considering the micro-support effect can improve the prediction of crack initiation sites based on 3D FE analysis.
- Based on the fatigue assessment, a notch-stress-based curve FAT 160 can be used with a critical distance of $d = 0.1$ mm and a microstructural length of $\rho^* = 0.4$ mm for specimens with severe weld imperfections.

The results of this study indicate that the accuracy of FE analysis can be improved by implementing the reverse engineering method to develop numerical models from 3D scans. Additionally, the prediction accuracy of crack initiation sites from the FE analysis can be enhanced by considering the micro-support effect.

Supplementary information The online version contains supplementary material available at https://doi.org/10.1007/s40194-025-02189-x.

Author contributions Mahamudul Hasan Tanvir: conceptualization, methodology, validation, formal analysis and investigation, writing—original draft, writing—review and editing, visualization.

Sulaiman Shojai: conceptualization, methodology, validation, writing—review and editing, resources.

Richard Banaschik: writing—review and editing, resources.

Moritz Braun: conceptualization, writing—review and editing, supervision.

Funding Open Access funding enabled and organized by Projekt DEAL.

Data availability Data are contained within the article. Further necessary information can be made available upon request.

Declarations

Conflict of interest The authors declare no competing interests.

References

1. Braun M, Ahola A, Milaković A-S, Ehlers S (2022) Comparison of local fatigue assessment methods for high-quality butt-welded joints made of high-strength steel. Forces in Mechanics 6:100056. https://doi.org/10.1016/j.finmec.2021.100056
2. Maddox SJ (2014) Fatigue strength of welded structures: Elsevier Ltd
3. Fricke W (2011) Fatigue strength assessment of local stresses in welded joints: Woodhead Publishing
4. Lassen T, Recho N (2006) Fatigue life analyses of welded structures. ISTE Ltd, London
5. Wang Q (2002) Effect of inclusion on subsurface crack initiation and gigacycle fatigue strength. Int J Fatigue 24(12):1269–1274. https://doi.org/10.1016/S0142-1123(02)00037-3
6. Bomas H, Schleicher M (2005) Application of the weakest-link concept to the endurance limit of notched and multiaxially loaded specimens of carburized steel 16MnCrS5. Fatigue Fract Eng Mater Struct 28(11):983–995. https://doi.org/10.1111/j.1460-2695.2005.00935.x
7. Alam MM, Barsoum Z, Jonsén P, Kaplan A, Häggblad H (2011) Influence of defects on fatigue crack propagation in laser hybrid welded eccentric fillet joint. Eng Fract Mech 78(10):2246–2258. https://doi.org/10.1016/j.engfracmech.2011.04.011
8. Frostevarg J, Kaplan AF (2014) Undercuts in laser arc hybrid welding. Phys Procedia 56:663–672. https://doi.org/10.1016/j.phpro.2014.08.071
9. Yukitaka M, Masahiro E (1983) Quantitative evaluation of fatigue strength of metals containing various small defects or cracks. Eng Fract Mech 17(1):1–15. https://doi.org/10.1016/0013-7944(83)90018-8
10. Zhang J, Li S, Yang Z, Li G, Hui W, Weng Y (2007) Influence of inclusion size on fatigue behavior of high strength steels in the gigacycle fatigue regime. Int J Fatigue 29(4):765–771. https://doi.org/10.1016/j.ijfatigue.2006.06.004
11. Alam MM, Barsoum Z, Jonsén P, Kaplan A, Häggblad H (2010) The influence of surface geometry and topography on the fatigue cracking behaviour of laser hybrid welded eccentric fillet joints. Appl Surf Sci 256(6):1936–1945. https://doi.org/10.1016/j.apsusc.2009.10.041
12. Kaffenberger M, Vormwald M (2012) Considering size effects in the notch stress concept for fatigue assessment of welded joints. Comput Mater Sci 64:71–78. https://doi.org/10.1016/j.commatsci.2012.02.047
13. Lang R, Lener G (2016) Application and comparison of deterministic and stochastic methods for the evaluation of welded

components' fatigue lifetime based on real notch stresses. Int J Fatigue 93:184–193. https://doi.org/10.1016/j.ijfatigue.2016.08.023

14. Stasiuk P, Karolczuk A, Kuczko W (2016) Analysis of correlation between stresses and fatigue lives of welded steel specimens based on real three-dimensional weld geometry. Acta Mech Autom 10(1):12–16. https://doi.org/10.1515/ama-2016-0002
15. He J, Wang H, Zhang Y (2024) Weld quality measurement of T-joints based on three-dimensional scanner. Int J Adv Manuf Technol 133(11–12):6059–6070. https://doi.org/10.1007/s00170-024-13847-7
16. Hegedűs-Kuti J, Szőlősi J, Varga D, Abonyi J, Andó M, Ruppert T (2023) 3D scanner-based identification of welding defects-clustering the results of point cloud alignment. Sensors (Basel) 23(5):2503. https://doi.org/10.3390/s23052503
17. ISO 12932 (2013) Welding–laser-arc hybrid welding of steels, nickel and nickel alloys-quality levels for imperfections
18. ISO 5817:2023: Welding—fusion-welded joints in steel, nickel, titanium and their alloys (beam welding excluded)—quality levels for imperfections
19. Hobbacher A, Kassner M (2012) On relation between fatigue properties of welded joints, quality criteria and groups in ISO 5817. Weld World 56(11–12):153–169. https://doi.org/10.1007/BF03321405
20. Lener G, Lang R, Ladinek M, Timmers R (2018) A numerical method for determining the fatigue strength of welded joints with a significant improvement in accuracy. Procedia Eng 213:359–373. https://doi.org/10.1016/j.proeng.2018.02.036
21. Niederwanger A, Warner DH, Lener G (2020) The utility of laser scanning welds for improving fatigue assessment. Int J Fatigue 140:105810. https://doi.org/10.1016/j.ijfatigue.2020.105810
22. Hou C (2019) Computer simulation of weld toe stress concentration factor sequence for fatigue analysis. IJSI 10(6):792–808. https://doi.org/10.1108/IJSI-11-2018-0086
23. Hou C (2007) Fatigue analysis of welded joints with the aid of real three-dimensional weld toe geometry. Int J Fatigue 29(4):772–785. https://doi.org/10.1016/j.ijfatigue.2006.06.007
24. Liinalampi S, Remes H, Lehto P, Lillemäe I, Romanoff J, Porter D (2016) Fatigue strength analysis of laser-hybrid welds in thin plate considering weld geometry in microscale. Int J Fatigue 87:143–152. https://doi.org/10.1016/j.ijfatigue.2016.01.019
25. Chaudhuri S, Crump J, Reed PAS, Mellor BG (2019) High-resolution 3D weld toe stress analysis and ACPD method for weld toe fatigue crack initiation. Weld World 63(6):1787–1800. https://doi.org/10.1007/s40194-019-00792-3
26. Stasiuk P, Karolczuk A, Kuczko W (2014) Analysis of non-uniform distribution of the equivalent stress by selected multiaxial fatigue criteria in butt-welded joint. Acta Mech Autom 8(2):79–82. https://doi.org/10.2478/ama-2014-0014
27. Kolios A, Wang L, Mehmanparast A, Brennan F (2019) Determination of stress concentration factors in offshore wind welded structures through a hybrid experimental and numerical approach. Ocean Eng 178:38–47. https://doi.org/10.1016/j.oceaneng.2019.02.073
28. Späth R, Steinebrunner M (2023) "Using 3D-scanners and finite element method to assess the fatigue life of welded joints based on the actual geometry of seam welds: realistic modelling of notches at the weld toe", (in en;de). Materialwiss Werksttech 54(4):459–465. https://doi.org/10.1002/mawe.202300020
29. Pomberger S, Stoschka M, Aigner R, Leitner M, Ehart R (2020) Areal fatigue strength assessment of cast aluminium surface layers. Int J Fatigue 133:105423. https://doi.org/10.1016/j.ijfatigue.2019.105423
30. Schneller W et al (2021) Fatigue strength assessment of additively manufactured metallic structures considering bulk and surface layer characteristics. Addit Manuf 40:101930. https://doi.org/10.1016/j.addma.2021.101930
31. Shojai S, Schaumann P, Braun M, Ehlers S (2022) Influence of pitting corrosion on the fatigue strength of offshore steel structures based on 3D surface scans. Int J Fatigue 164:107128. https://doi.org/10.1016/j.ijfatigue.2022.107128
32. Shojai S, Schaumann P, Brömer T (2022) Probabilistic modelling of pitting corrosion and its impact on stress concentrations in steel structures in the offshore wind energy. Mar Struct 84:103232. https://doi.org/10.1016/j.marstruc.2022.103232
33. ISO (2014) 6520–1:2007: welding and allied processes—classification of geometric imperfections in metallic materials—part 1: fusion welding. International Organization for Standardization: Geneva, Switzerland
34. Merkblatt DVS 2403 (2019) Empfehlungen für die Durchführung, Auswertung und Dokumentation von Schwingfestigkeitsversuchen an Schweißverbindungen metallischer Werkstoffe
35. Hobbacher AF (2016) Recommendations for fatigue design of welded joints and components. Springer International Publishing, Cham
36. Taylor D (2008) The theory of critical distances. Eng Fract Mech 75(7):1696–1705. https://doi.org/10.1016/j.engfracmech.2007.04.007
37. Taylor D (2011) Applications of the theory of critical distances in failure analysis. Eng Fail Anal 18(2):543–549. https://doi.org/10.1016/j.engfailanal.2010.07.002
38. Taylor D, Bologna P, Bel Knani K (2000) Prediction of fatigue failure location on a component using a critical distance method. Int J Fatigue 22(9):735–742. https://doi.org/10.1016/S0142-1123(00)00062-1
39. Shojai S, Schaumann P, Ghafoori E (2024) Micro-support effect consideration in fatigue analysis of corroded steel based on real surface geometry. J Constr Steel Res 212:108259. https://doi.org/10.1016/j.jcsr.2023.108259
40. Peterson (1959) Notch sensitivity. In Metal Fatigue. pp 293–306
41. Neuber H (1968) Über die Berücksichtigung der spannungskonzentration bei festigkeitsberechnungen
42. Baumgartner J, Schmidt H, Ince E, Melz T, Dilger K (2015) Fatigue assessment of welded joints using stress averaging and critical distance approaches. Weld World 59(5):731–742. https://doi.org/10.1007/s40194-015-0248-x
43. Sonsino CM, Bruder T, Baumgartner J (2010) S-n lines for welded thin joints — suggested slopes and FAT values for applying the notch stress concept with various reference radii. Weld World 54(11–12):R375–R392. https://doi.org/10.1007/BF03266752